The final publication is available at

https://doi.org/10.1016/j.cattod.2016.08.008

Additional Information

TiO$_2$ polymorph dependent SMSI effect in Co-Ru/TiO$_2$ catalysts and its relevance to Fischer-Tropsch synthesis

Francine Bertella [a,b], Patricia Concepción [a], Agustín Martínez [a,*]

[a] *Instituto de Tecnología Química, Universitat Politècnica de València - Consejo Superior de Investigaciones Científicas, Avda. de los Naranjos s/n, 46022 Valencia, Spain*

[b] *CAPES Foundation, Ministry of Education of Brazil, 70040-020 Brasilia-DF, Brazil*

* Corresponding author: amart@itq.upv.es (A. Martínez)

Abstract

Pure anatase and rutile TiO_2 samples were synthesized by thermal treatment of reverse microemulsions and applied as supports for preparing Ru-promoted Co catalysts (0.5 wt% Ru, 10 wt% Co). The catalysts were characterized by ICP-OES, XRD, Raman spectroscopy, N_2 physisorption, H_2-TPR, electron microscopy (FESEM, HAADF-STEM), H_2 chemisorption, XPS, and *in situ* IR-CO after H_2 reduction and reaction with syngas, and their catalytic performance for Fischer-Tropsch synthesis (FTS) studied at industrial conditions (220 °C, 2.0 MPa, H_2/CO= 2). The two catalysts exhibited comparable mean Co particle sizes (5-6 nm) as well as high and alike degrees of cobalt reduction (ca. 90%). The SMSI decoration effect arising during H_2 reduction was much more pronounced for the anatase-supported catalyst resulting in lower cobalt-time-yield (CTY) compared to that supported on TiO_2-rutile. *In situ* IR-CO under syngas conversion conditions showed equivalent cobalt surface reconstruction and nature of the surface Co^0 sites for both catalysts in their *working* state, and revealed a partial reversibility of the SMSI effect during FTS by which a significant fraction of the decorated Co^0 centers in the anatase-based catalyst was uncovered and became available for reaction. The implication of this effect on TOFs is discussed. The C_{5+} selectivity was higher for the rutile-based catalyst, although a clear impact of the SMSI effect on selectivities was not inferred from our results.

Keywords: Fischer-Tropsch synthesis; cobalt catalyst; TiO_2 polymorph; anatase; rutile; SMSI effect.

1. Introduction

Fischer-Tropsch synthesis (FTS) is at the core of XTL processes allowing a variety of liquid fuels and chemicals to be produced from oil-alternative carbon resources such as natural gas (GTL), coal (CTL), and biomass (BTL) via syngas (H_2+CO). Of particular interest is the Co-catalyzed low-temperature FTS in which syngas is selectively converted to long-chain *n*-paraffins (waxes) that are then hydrocracked to produce high-quality diesel [1, 2].

Preparation of Co-based FTS catalysts commonly involves dispersion (via impregnation) of a cobalt salt precursor, most frequently cobalt nitrate, on a high surface area porous inorganic oxide carrier, among which SiO_2, Al_2O_3, and TiO_2 are the most widely employed, followed by drying, calcination, and H_2-reduction to generate the active metallic Co sites on the catalyst surface [1]. Commonly, some metals (e.g. Ru, Re, Pt) and/or metal oxides are included in the catalyst formulation in order to promote the reduction and dispersion of the supported Co particles [3, 4]. The final catalytic performance of Co-based FTS catalysts becomes mainly dictated by the metal content, the dispersion (i.e. Co particle size), and the degree of Co reduction which ultimately determine the concentration of surface metal Co sites. These properties are affected by a number of factors such as the nature of the cobalt precursor and loading method [1], the chemical identity and porosity of the oxide carrier [1, 5, 6], and the so-called thermal history (i.e. the drying, calcination, and reduction conditions) [7].

As for the chemical nature of the support, TiO_2 has proven to be particularly beneficial from the standpoint of both catalyst activity and selectivity to the targeted liquid (C_{5+}) hydrocarbon fraction [6, 8, 9]. As a support, TiO_2 is known to exhibit the SMSI (strong-metal-support-interaction) decoration effect by virtue of which TiO_{2-x} sub-oxides form during H_2 reduction and migrate on top of the supported metal nanoparticles inhibiting their H_2 and CO chemisorption capability [10-14]. For Co/TiO_2, partial encapsulation of Co nanoparticles by a few atomic layers of thick TiO_{2-x} phase during reduction was directly imaged by HRTEM [15]. In nature, TiO_2 exists in three distinct crystallographic forms, namely anatase, rutile, and brookite. Previous studies have shown that the TiO_2 crystal phase composition is highly influential to the ultimate FTS performance of Co/TiO_2 catalysts, albeit with controversial results. For instance, by supporting 20 wt% Co on TiO_2 with different anatase:rutile ratios, Jongsomjit et al. observed a maximum CO conversion rate under methanation conditions (H_2/CO= 10) for the catalyst comprising 19% rutile and 81% anatase which also exhibited the

3

highest H_2 chemisorption capacity [16]. This behavior was ascribed to a weaker interaction of Co with rutile in comparison to anatase that prevented the formation of barely reducible mixed Co-O-Ti compounds assisted by water generated during the H_2 reduction treatment thus increasing the amount of available surface Co^0 atoms [17]. Other authors also reported higher CO conversion rates for Co/TiO_2 catalysts prepared from TiO_2 with more than 15% rutile in comparison to those based on pure anatase [18, 19]. However, in contrast with the previous study, the effect was related to a stronger Co-support interaction in presence of rutile that inhibited the aggregation of Co particles during reduction improving the final Co^0 dispersion, although the possibility of a suppressed SMSI effect over rutile was not excluded [18].

It is apparent from the previous discussion that further work is required to clarify the role of the TiO_2 crystalline phase, with a special focus on the little studied phase-dependent SMSI effect, in determining the FTS performance of Co/TiO_2 catalysts. To this aim, we synthesized 100% pure anatase and rutile TiO_2 phases and used them as supports for preparing Ru-promoted Co/TiO_2 catalysts (nominal loadings of 10 wt% Co and 0.5 wt% Ru). The prepared catalysts display alike mean Co^0 particle sizes (5-6 nm) and particle size distributions as well as high and similar extents of cobalt reduction (ca. 90%), enabling a fair study of the TiO_2 crystalline phase dependent SMSI effect and its consequences on the catalytic behavior for FTS under industrially relevant conditions (220 °C , 2.0 MPa, H_2/CO= 2).

2. Experimental

2.1. Materials

Triton X-100 [(*tert*-octylphenoxy)polyethoxyethanol] (Aldrich), titanium(IV) butoxide (99+%, Alfa Aesar), 1-hexanol (>98% GC, Fluka Chemika), cyclohexane (99%, Aldrich), hydrochloric acid (37%, Aldrich), and acetic acid (99,5%, Aldrich) were used as received.

2.2. Synthesis of pure anatase and rutile TiO_2 phases

Pure anatase and rutile TiO_2 phases were synthesized by thermal treatment of reverse microemulsions following a procedure similar to that reported in [20]. In short, an aqueous solution containing the acid (acetic acid for anatase and hydrochloric acid for rutile) and the Ti source (titanium(IV) butoxide) was added to an organic mixture containing the surfactant (Triton X-100), cosurfactant (1-hexanol), and solvent (cyclohexane) under stirring

at room temperature (r.t.). The formed microemulsion was then either heated at 40 °C for 24 h under reflux (for rutile) or introduced into a Teflon-lined stainless steel autoclave and hydrothermally treated at 120 °C for 5 h (for anatase). After the thermal treatments the solids were recovered by centrifugation, washed 5 times in ethanol in a process involving redispersion and centrifugation, dried at 60 °C overnight, and finally calcined in flowing air at 400 °C for 8 h. The obtained TiO_2 anatase and rutile supports are labeled as Ti-A and Ti-R, respectively. The conditions and composition of the microemulsions employed for the syntheses of pure anatase and rutile phases are gathered in Table 1.

Table 1

2.3. Synthesis of Co-Ru/TiO$_2$ catalysts

Co-Ru/TiO_2 catalysts with nominal loadings of 10 wt% Co and 0.5 wt% Ru (added as reduction promoter) were prepared by incipient wetness co-impregnation of the calcined TiO_2 carriers with an aqueous solution of $Co(NO_3)_2 \cdot 6H_2O$ (Aldrich) and ruthenium(III) nitrosyl nitrate (Aldrich) as metal precursors, followed by drying at 100 °C overnight and calcination in flowing air at 300 °C for 3 h. The catalysts based on anatase and rutile are denoted as Co-Ru/Ti-A and Co-Ru/Ti-R, respectively.

2.4. Characterization techniques

X-ray powder diffraction (XRD) patterns were recorded on a Philips X'Pert diffractometer using monochromatic Cu K$_\alpha$ radiation (λ= 0.15406 nm). The average TiO_2 crystallite size was estimated by the Scherrer's equation applied to the most intense reflections (1 1 0) for rutile (2θ= 27.44°) and (1 0 1) for anatase (2θ= 25.28°), assuming a shape factor k= 0.9.

Textural properties were derived from the N_2 adsorption isotherms measured at -196 °C in an ASAP-2420 equipment (Micromeritics). Specific surface areas were calculated following the Brunauer–Emmett–Teller (BET) method, total pore volumes (TPV) were determined at a relative pressure of 0.98, and the pore size distributions were obtained by applying the Barrett–Joyner–Halenda (BJH) approach. Prior to the adsorption measurements, the samples were degassed at 300 °C and vacuum overnight.

The morphology of the samples were studied by field emission scanning electron microscopy (FESEM) using a ZEISS Ultra-55 microscope.

The Co and Ru contents were determined by ICP-OES (Inductively Coupled Plasma-Optical Emission Spectrometry) in a Varian 715-ES spectrometer after dissolution of the solids in an acid mixture of 20%HNO_3:20%HF:60%HCl (% volume).

The reduction behavior of the oxidized Co-Ru/TiO_2 catalysts was studied by hydrogen temperature-programmed reduction (H_2-TPR) in a Micromeritics Autochem 2910 equipment. The samples were initially flushed with an Ar flow at r.t. for 30 min, and then the gas was switched to 10 vol% H_2 in Ar and the temperature linearly increased up to 900 °C at a heating rate of 10 °C/min. A downstream 2-propanol/$N_{2(liq)}$ trap was used to retain the water generated during the reduction. The H_2 consumption rate was monitored in a thermal conductivity detector (TCD) previously calibrated using the reduction of a standard CuO sample. This setup was also used to measure the degree of cobalt reduction (DR) after submitting the catalysts to the same reduction protocol applied *in-reactor* prior to the FTS experiments (400 °C in H_2 flow for 10 h).

Cobalt dispersions were determined by H_2 chemisorption at 100 °C in an ASAP 2010C Micromeritics equipment by extrapolating the total H_2 uptake to zero pressure [21]. Metal particle sizes (d(Co^0)$_{H2}$) were estimated from the total amount of chemisorbed H_2, the Co content (from ICP-OES) and the degree of cobalt reduction by assuming a chemisorption stoichiometry H/Co= 1 and a surface atomic density for Co^0 of 14.6 atoms/nm^{-2}.

Cobalt particle sizes were studied by electron microscopy in a JEOL-JEM-2100F microscope operating at 200 kV in scanning-transmission mode (STEM) using a High-Angle Annular Dark Field (HAADF) detector. Prior to microscopy observation, the samples were suspended in ethanol and submitted to ultrasonication for one minute. Afterwards, the suspension was let to slowly decant for two minutes and a drop was extracted from the top side and placed on a carbon-coated copper grid. The catalysts were previously *ex situ* reduced under a flow of H_2 at 400 °C, passivated at r.t. under a flow of 0.5% O_2/N_2, and stored at r.t. until the sample preparation for microscopy. Metal particle size histograms were generated upon measurement of 150–200 particles from several micrographs taken at different positions on the TEM grid. Metallic cobalt particle sizes (d(Co^0)$_{TEM}$) were corrected for a 3 nm thick CoO passivation outlayer [22].

X-ray photoelectron spectra (XPS) were collected using a SPECS spectrometer with a 150MCD-9 detector and using a non-monochromatic Mg Kα (1253.6 eV) X-ray source. Spectra were recorded using an analyzer pass energy of 30 eV, an X-ray power of 200 W, and an operating pressure of 10^{-9} mbar. During data processing of the XPS spectra, binding energy (BE) values were referenced to the Ti2p peak (458.6 eV). Spectra treatment was performed using the CASA software. The samples were analysed in their calcined state as well as after H_2 reduction (20 cm^3/min) at 400 °C for 2 h in a micro-reactor directly connected to the UHV of the XPS analyse chamber to avoid contact with air after the sample treatment.

IR-CO spectra were recorded with a Nexus 8700 FTIR spectrometer using a DTGS detector and acquiring at 4 cm^{-1} resolution. An IR cell allowing *in situ* treatments in controlled atmospheres and temperatures in the 25-500 °C range was connected to a vacuum system with gas dosing facility. For IR studies, previously reduced (at 400 °C for 10 h) and passivated samples were pressed into self-supported wafers of 10 mg/cm^2 and reduced again in the IR cell at 400 °C in H_2 flow (20 cm^3/min) for 2 h, followed by vacuum treatment at 450 °C for 1 h. Afterwards, the samples were cooled down to 25 °C under dynamic vacuum and CO was dosed at increasing pressures (1.9-30 mbar). IR spectra were recorded after each dosage. Additional *in situ* IR experiments were performed by exposing the reduced catalysts to a flow of syngas (50 cm^3/min) at r.t. for 1 h to ensure homogeneous atmosphere in the IR cell. Next, the temperature was increased up to the FTS reaction temperature of 220 °C and the spectra recorded after 4 h of reaction at this condition. Spectra analysis was done using the Origin software.

2.5. Fischer–Tropsch synthesis experiments

Fischer–Tropsch synthesis (FTS) experiments were performed in a down-flow fixed bed stainless steel reactor with i.d. of 10 mm and length of 40 cm. The reactor was loaded with 0.5 g of catalyst (0.25–0.42 mm pellet size) diluted with SiC granules (0.6–0.8 mm) until a total bed volume of 6.4 cm^3. The catalysts were reduced *in situ* in flowing H_2 at 400 °C for 10 h at ambient pressure. After reduction, the temperature was decreased to 100 °C under flow of H_2 and then *syngas* with H_2/CO molar ratio of 2 (CO:H_2:Ar volume ratio of 3:6:1, Ar as internal standard for gas chromatography) was flowed through the reactor at the desired flow rate, the reaction pressure increased up to 2.0 MPa, and the temperature raised up to

220 °C at a rate of 2 °C/min. The temperature in the catalytic bed was controlled by two thermocouples connected to independent PID controllers, while a third vertically sliding thermocouple was used to verify the absence of temperature gradients (T= 220 $\pm$1 °C) along the catalyst bed. Initial FTS activities were determined at *quasi*-differential CO conversions (< 10%) using a constant gas hourly space velocity (GHSV) of 11.7 $L_{syngas}/(g_{cat} \cdot h)$ to ensure a low water partial pressure in the catalytic bed. This condition was maintained during ca. 7 h on stream, after which the GHSV was adjusted for each catalyst so as to attain a constant CO conversion of 10 $\pm$ 2% in the *pseudo*-steady state. Heavier hydrocarbons were condensed in two consecutive traps located at the reactor outlet and kept, respectively, at 150 °C and 100 °C, both at the reaction pressure (2.0 MPa). The stream leaving the second trap was depressurized and regularly analyzed *on line* in a Varian 450 gas chromatograph (GC) equipped with three columns and TCD and FID detectors. After separation of the water co-product, the hydrocarbon fractions collected in the traps were weighted, diluted with CS_2, and analyzed *off line* in the same GC. The combination of the *on line* and *off line* GC analyses through the common product methane resulted in carbon mass balances in the 98-102% range. Product selectivities are expressed on a carbon basis.

3. Results and discussion

3.1. Characterization of the TiO_2 supports

The XRD patterns of the calcined supports (Fig. 1) confirm the successful synthesis of 100% pure anatase (JCPDS 00-021-1272) and rutile (JCPDS 00-021-1276) phases at the specific microemulsion conditions employed. This phase selectivity is closely related to the type of acid used [23-25], and originates from the different affinities of the acids with the octahedral TiO_6 units during the phase transformation from anatase to rutile. Hence, CH_3COO^- anions coordinate stronger to titanium than Cl^- anions, preventing the transformation of the metastable anatase phase to the thermodynamically more stable rutile form [25, 26]. No other crystalline phases were detected. Line broadening analysis of the most intense reflections using the Scherrer's approach reveals a lower mean particle size for anatase (9.5 nm) compared to rutile (13.6 nm), as shown in Table 2.

Figure 1

Table 2

The N_2 adsorption isotherms and the pore size distributions for the TiO_2 carriers are shown in Fig. 2, and the derived textural properties are summarized in Table 2. The Ti-A sample presents a type IV adsorption isotherm characteristic of mesoporous solids, while Ti-R exhibits type III adsorption isotherm typical for non-porous or macroporous solids (Fig. 2a) [27]. At high relative pressures (> 0.95) both samples show a rapid increase in the amount of N_2 adsorbed that signs for the presence of large interparticle mesopores and macropores, particularly in the rutile Ti-R sample. The N_2 uptake capacity is much higher for the anatase sample which, accordingly, displays notably higher specific surface area (BET= 164 m^2/g) and total pore volume (TPV= 0.30 cm^3/g) than rutile (BET= 59 m^2/g, TPV= 0.17 cm^3/g, Table 2). In turn, the anatase support shows a relatively narrow unimodal pore size distribution in the mesopore range (2-20 nm) with a maximum centered at 8.8 nm. Differently, the rutile sample displays a very broad pore size distribution with a maximum at 7.4 nm and a profile extending beyond the range of mesopores that can be reliably measured by N_2 physisorption (Fig. 2b). This reflects the presence of large mesopores and macropores in this sample already inferred from the shape of the N_2 adsorption isotherm at high P/P_0 values. The average pore diameter (BJH) is 6.4 nm for Ti-A and 7.3 nm for Ti-R (Table 2). However, the total pore volume and average pore diameter for the rutile sample are probably underestimated due to the inadequacy of N_2 to measure the larger mesopores and macropores present in this material.

Figure 2

As for the morphology, the FESEM images in Fig. 3 show irregularly-shaped agglomerates of small rice-like crystallites sizing about 10-30 nm for anatase (Fig. 3a) and pseudo-spherical agglomerates (0.2-0.5 μm) of slightly elongated crystallites (10-20 nm) for rutile (Fig. 3b). The observed differences in morphology are mainly dictated by the type of acid employed in the syntheses [28], although other factors like the concentration of the Ti source in the microemulsion may be also influential [29, 30].

Figure 3

3.2. Characterization of the Co-Ru/TiO$_2$ catalysts

3.2.1. Structural and textural properties

The XRD patterns of the calcined Co-Ru/TiO$_2$ catalysts are shown in Fig. 4. The mean particle size of the TiO$_2$ supports did not experience significant variations upon impregnation with the metal precursors and calcination. Besides TiO$_2$ peaks, reflections belonging to the Co$_3$O$_4$ spinel phase (JCPDS 00-042-1467) are clearly perceived in the calcined catalysts, with no signs for the presence of other crystalline cobalt phases. However, the relatively low intensity of the spinel peaks and overlapping with TiO$_2$ diffractions prevent an accurate estimation of the Co$_3$O$_4$ crystallite sizes by line broadening analysis. Moreover, formation of mixed Co-Ti compounds (e.g. CoTiO$_3$) was not evidenced by Raman spectroscopy for any of the two studied catalysts, as shown in Fig. S1 of the Supplementary Material, although their presence cannot be completely excluded.

Figure 4

The Co content in the catalysts determined by ICP-OES slightly exceeds the nominal value (11-12 wt%) while the concentration of Ru (0.3-0.4 wt%) is 20-40% lower than the expected value (Table 3). The partial loss of Ru upon air-calcination has been previously reported and is attributed to the formation of volatile suboxide RuO$_x$ species under oxidizing atmospheres [31-33].

The Co-Ru/TiO$_2$ catalysts exhibit N$_2$ adsorption isotherms similar to the respective supports, albeit with a decreased N$_2$ adsorption capacity due to the deposited metal oxide phases (Fig. 5a). Analogously to the respective supports, the catalyst based on rutile shows a much broader pore size distribution than that based on anatase which, differently, displays a rather narrow distribution with a maximum for pores sizing ca. 8.1 nm (Fig. 5b). The textural properties derived from the N$_2$ adsorption isotherms are collected in Table 3. The BET area of the catalysts decreases by 23-28% and the total pore volume (TPV) by 18-23% relative to the pristine supports. However, when calculated per mass of TiO$_2$ support (Table 3) the relative decreases in BET area and TPV are, respectively, 8% and 10% for the anatase-based catalyst and 15% and 6%, respectively, for the catalyst supported on rutile. Therefore, considering the dilution effect, these results suggest a minor pore blockage ($\leq$ 10%) by the

supported metal oxides, particularly in the rutile-based catalyst presenting wider pores. In turn, no significant variations in the mean pore diameter are noticed for the catalysts with respect to the corresponding supports (Table 3).

Figure 5

Table 3

3.2.2. Reducibility and particle size of cobalt

The reduction behavior of the Co-Ru/TiO$_2$ catalysts was studied by H$_2$-TPR, and the corresponding reduction profiles are shown in Fig. 6. No appreciable H$_2$ consumption was observed for the pristine Ti-A and Ti-R supports, in agreement with previous reports [16, 34, 35]. Both catalysts display two main reduction features with maximum H$_2$ consumptions (T$_{max}$) at ca. 120-190 °C and 260-350 °C, respectively, that correspond to the stepwise reduction of Co$_3$O$_4$ to metallic Co (Co$_3$O$_4$ → CoO → Co^0) as commonly observed for *ex*-nitrate supported Co catalysts [5, 33, 36]. Besides, an additional reduction with lower H$_2$ consumption is perceived at higher temperatures (T$_{max}$ at 390 °C for Co-Ru/Ti-A and 425 °C for Co-Ru/Ti-R) which can be ascribed to the reduction of oxidic Co phases presenting a stronger interaction with the TiO$_2$ support. Moreover, a relatively small H$_2$ consumption extending over a broad temperature range (500-700 °C) is inferred for the Co-Ru/Ti-A sample. This feature might be related to the reduction of minor amounts of mixed Co-O-Ti compounds, although a contribution from the partial reduction of anatase TiO$_2$ assisted by metallic Co (and Ru) species via H$_2$ spillover is not discarded. It is clearly seen in Fig. 6 that the T$_{max}$ for the main reductions are downward shifted by ca. 70-90 °C in the Co-Ru/Ti-A sample in comparison to Co-Ru/Ti-R, signing for an enhanced reducibility of cobalt when supported on anatase. An easier reducibility, hence a weaker Co-support, for Co oxides supported on anatase was also concluded by Shimura et al. in previous studies using TiO$_2$ supports with different % fraction of rutile phase [18, 19], although the opposite trend (i.e. a weaker Co-support interaction for rutile) was reported by others [16, 17, 37]. Nonetheless, a high degree of cobalt reduction can be anticipated after the pre-catalysis reduction treatment with pure H$_2$ at 400 °C for 10 h at the view of the corresponding profiles, as expected from the presence of the Ru reduction promoter [38-43]. In fact, degrees of cobalt

reduction (DR) of 89-93% were obtained from the H_2 consumed in H_2-TPR experiments performed on catalysts pre-reduced at 400 °C for 10 h in pure H_2 (see section 2.4), as shown in Table 4. Such high and alike DR values are desirable not only to maximize the amount of active Co^0 sites but also to avoid potential side effects on the FTS activity and selectivity due to the presence of oxidic Co species supported on TiO_2, as recently reported [44]. A high extent of reduction of Co_3O_4 to Co^0 in the CoRu/TiO_2 catalysts is also concluded from *in situ* H_2-XRD experiments, which indicated the presence of both *hcp-* and *fcc-*Co^0 with no evidence for Co_3O_4 or CoO crystalline phases after the *in situ* treatment at 400 °C (7 h) in flowing H_2 (see Fig. S2 in Supplementary Material). Additionally, no signs for the formation of Co-Ti alloys or mixed oxides were found in these experiments.

Figure 6

Table 4

The H_2 uptakes obtained from H_2 chemisorption and the mean Co^0 particle sizes estimated from both H_2 chemisorption (d(Co^0)$_{H2}$) and TEM (d(Co^0)$_{TEM}$) are also included in Table 4. As seen there, the H_2 uptake for Co-Ru/Ti-A is about 50% that of Co-Ru/Ti-R. The obtained H_2 uptakes translate into "apparent" Co^0 particle sizes (d(Co^0)$_{H2}$) of ca. 65 nm and 30 nm for the catalysts supported on, respectively, anatase and rutile phases. On the other hand, the size of the supported Co^0 nanoparticles was also obtained by direct electron microscopy imaging of as-reduced samples. Representative HAADF-STEM images and the corresponding particle size histograms are shown in Fig. 7. Metallic Co nanoparticles, appearing as bright spots in the micrographs, look relatively well distributed over the two TiO_2 supports, although some clustered regions can be perceived, as commonly observed for supported Co catalysts prepared by impregnation using cobalt nitrate precursor [45, 46]. The histograms reveal similar Co^0 particle size distributions spanning from ca. 2 to 14 nm, with predominance of nanoparticles sizing 4-6 nm. Nonetheless, the rutile-based catalyst presents a somewhat greater contribution from particles above 8 nm in diameter (Fig. 7d) which results in a slightly higher average Co^0 particle size (6.0 nm) in comparison to the anatase-supported sample (5.2 nm), as seen in Table 4. The formation of some larger Co^0 nanoparticles in Co-Ru/Ti-R can be related to the presence of wider pores in the rutile

support (Fig. 2) in which the nanoparticles may grow in a less constrained environment [47-52].

Figure 7

The significantly greater "apparent" Co^0 particle sizes obtained from H_2 chemisorption measurements with respect to those derived from statistical TEM analysis is a clear sign for the occurrence of the SMSI effect during the H_2 reduction treatment at 400 °C, as it is well documented for cobalt (as well as other metals) supported on TiO_2 [10-15]. As a consequence, the H_2 (and CO) chemisorption capacity of metallic cobalt is suppressed by TiO_{2-x} species that migrate from the support and decorate the nanoparticles. The remarkably lower H_2 uptake observed for Co-Ru/Ti-A hence indicates that the SMSI decoration effect occurred to a greater extent when Co is supported on anatase in comparison to rutile. This conforms with earlier studies which reported the occurrence of SMSI in Pd supported on anatase but not on rutile after reduction in H_2 at a relatively low temperature of 200 °C [53].

3.2.3. Surface properties of cobalt

The surface properties of cobalt in the Co-Ru/Ti-A and Co-Ru/Ti-R catalysts have been studied by XPS and IR of adsorbed CO. The surface Co/Ti atomic ratio in the calcined samples as measured by XPS is 0.08 for Co-Ru/Ti-A and 0.24 for Co-Ru/Ti-R (Table 4), evidencing a higher dispersion of the Co_3O_4 oxide phase in the catalyst supported on rutile TiO_2. The $Co2p_{3/2}$ XP spectra for the calcined catalysts are presented in Fig. 8a. Deconvolution of the $Co2p_{3/2}$ core level in the spectrum of the calcined Co-Ru/Ti-A sample shows two main components at 779.0 and 780.7 eV with a broad satellite structure at 786.3 eV characteristic for the spinel Co_3O_4 oxide [54]. These peaks appear shifted to higher binding energies (780.0 and 781.7 eV, with a satellite structure at 786.9 eV) in the Co-Ru/Ti-R sample. Moreover, the intensity of the satellite peak (distinctive of paramagnetic Co^{2+} species [55-57]) relative to the main peak is higher in Co-Ru/Ti-R (s/m= 0.383) than in Co-Ru/Ti-A (s/m= 0.215). Thus, both the lower BE of the $Co2p_{3/2}$ peaks and the lower s/m ratio obtained for the catalyst supported on TiO_2-anatase suggest a higher fraction of surface Co^{3+} sites (i.e. surface defects) in this catalyst relative to that supported on TiO_2-rutile. Unlike the oxidized samples, analogous $Co2p_{3/2}$ core level profiles (Fig. 8b) and surface Co/Ti atomic ratios (ca. 0.3, Table

13

4) were observed for Co-Ru/Ti-A and Co-Ru/Ti-R after H_2 reduction. The much higher increase in the surface Co/Ti atomic ratio observed for the anatase-based catalyst upon H_2 reduction is indicative of a higher mobility of the titanium species in this polymorph. The deconvoluted spectra in Fig. 8b show components at 777.5 eV, 779.1 eV, 780.8 eV, 783.2 eV, and 786.8 eV. The 777.5 eV peak is ascribed to metallic cobalt. In turn, the presence of the peak at 780.8 eV of oxidized cobalt species (and the corresponding shake-up satellite structures at 783.2 and 786.8 eV) evidences a less effective reduction of Co_3O_4 to Co^0 in the *in situ* H_2 treatment at 400 °C for 2 h (ca. 25% of Co^0 in both samples) in comparison to the high reduction degrees (~90%) achieved in the pre-catalysis H_2 reduction at 400 °C for 10 h. The assignment of the component at 779.1 eV exhibiting a BE intermediate between Co^0 and Co^{2+} is less straightforward. De la Peña O'Shea et al. attributed a similar component in Co/TiO_2 samples to the formation of Co-O-Ti linkages during the reduction treatment arising from the SMSI decoration effect [15]. However, the comparable relative contribution of this component in the XPS spectra of the as-reduced catalysts (Fig. 8b) seems inconsistent with its attribution to Co-O-Ti species originated only from the SMSI effect which occurs to a much greater extent in the catalyst supported on anatase TiO_2. Thus, we suggest that the component at 779.1 eV is contributed not only from the SMSI effect but also from cobalt species at the perimeter of the nanoparticles in close contact with the TiO_2 support.

Figure 8

The fact that XPS, with a penetration depth of ca. 6 nm, did not reveal appreciable differences in the state of the cobalt in the as-reduced samples suggests that the SMSI effect should occur on the uppermost layers of the Co^0 nanoparticles. Therefore, we studied the properties of the surface Co^0 sites by means of a more surface-sensitive technique such as IR spectroscopy of adsorbed CO. The IR-CO spectra recorded at r.t. for increasing CO doses are presented in Fig. 9. In the case of Co-Ru/Ti-R, IR bands at 2073, 2063, 2047, and 2014 cm^{-1} are clearly observed (Fig. 9a), which are assigned to CO interacting with both *fcc* and *hpc* Co^0 crystal phases (bands in the 2073-2047 cm^{-1} range [58]) and with coordinatively unsaturated Co^0 sites in defects of the metal crystallites such as edges, steps, and corners (band at 2014 cm^{-1}) [22]. Differently, the reduced Co-Ru/Ti-A sample features much less intense bands at a lower frequency (2057 and 1994 cm^{-1}, Fig. 9b) that have been associated to defected Co^0

sites in a less extended surface crystal phase or to CO interacting in a *tilted* configuration with surface species at the metal-oxide interface [59]. In our case, the low frequency of the IR bands observed in the Co-Ru/Ti-A sample coupled to their low intensity is consistent with the presence of cobalt sites partially covered by TiO_{2-x} species and, thus, with a higher extent of the SMSI effect in this catalyst, as also concluded from other characterizations previously discussed.

Figure 9

Therefore, the different extent of the SMSI effect arising from the distinct TiO_2 crystal phase leads not only to a different concentration of exposed Co^0 sites but also to a dissimilar surface topology of the supported Co^0 nanoparticles. The implications of these effects on the catalytic performance of the Co-Ru/TiO$_2$ catalysts for FTS are discussed in the next section.

3.3. Fischer-Tropsch synthesis on Co-Ru/TiO$_2$ catalysts

3.3.1. FTS activity

The initial and *pseudo*-steady state CO conversions, cobalt-time-yields (CTYs), and turnover frequencies (TOFs) of the catalysts are presented in Table 5. The initial activities were estimated by extrapolation of the conversion-TOS curves at TOS= 0 (not shown). Clearly, the rutile-based catalyst displays a notably higher (by a factor of ca. 1.7) initial CO conversion and CTY than that supported on anatase. In the *pseudo*-steady state, the CTY$_{rutile}$/CTY$_{anatase}$ ratio at similar CO conversion (10 $\pm$ 1%) increases further to 2.1 (Table 5). Other authors also found a higher CO hydrogenation activity for rutile-containing Co/TiO$_2$ catalysts in comparison to those based on pure anatase [18, 19]. The enhanced activity in the presence of rutile phase was ascribed to an increase in the concentration of metallic surface Co sites (i.e. of Co^0 surface area) upon H$_2$ reduction, although with conflicting explanations. Thus, while some authors attributed the increase in the amount of accessible Co^0 sites in rutile-containing catalysts to a weaker Co-support interaction that increased the reducibility of Co [17], others indicated a stronger Co-support interaction that inhibited Co aggregation during the H$_2$ reduction process [18]. Our characterization results clearly evidenced an easier reduction of Co oxides to metallic Co in the anatase-supported catalyst

(Fig. 6). Nonetheless, the promotion of Co with Ru ensured a high and homogeneous degree of cobalt reduction (ca. 90%) for both catalysts after the H_2 reduction treatment at 400 °C for 10 h. Taking into account the similar TEM-derived Co^0 particle sizes (5-6 nm, Table 4) and degrees of cobalt reduction, the higher FTS activity of Co-Ru/Ti-R with respect to Co-Ru/Ti-A can be mainly ascribed to the higher H_2 chemisorption capacity (hence, higher amount of active surface Co^0 sites) of the rutile-based sample (Table 4) due to a suppressed SMSI decoration effect.

Table 5

Moreover, it can be observed in Table 5 that both catalysts exhibit similar TOFs (based on H_2 chemisorption) both at initial (ca. $9\text{-}11 \cdot 10^{-2}$ s^{-1}) and steady state (ca. $6.5 \cdot 10^{-2}$ s^{-1}) conditions. These values are in the range of TOFs reported for *ex*-nitrate Co catalysts supported on SiO_2 [7], γ-Al_2O_3 [5, 33], and TiO_2 [5, 60, 61] at equivalent reaction conditions (220 °C, 2.0 MPa). In the cobalt-catalyzed FTS, a dependence of TOF with Co^0 particle size has been unambiguously proved for Co supported on carbon nanofibers [62] and silica [22] materials by which TOF drastically drops for metal particle sizes below 6-8 nm and remains invariable for larger particle sizes. In the case of TiO_2-supported catalysts, the effect of Co^0 particle size on TOF is less clear, probably due to the difficulty for preparing appropriate model catalysts. For instance, Delgado et al. observed an increase in TOF when decreasing the particle size from 7 to 1.7 nm in TiO_2-supported colloidal cobalt nanoparticles synthesized in water by chemical reduction with $NaBH_4$ [63]. Liu et al. also suggested a higher intrinsic activity for Co^0 nanoparticles sizing less than 10 nm when supported on β-SiC coated with TiO_2 [64]. The results from these studies appear thus to contradict the TOF-particle size trend reported for small (< 10 nm) cobalt nanoparticles supported on carbon and silica materials, and advises for further studies to elucidate Co particle size effects in TiO_2-supported catalysts. Nonetheless, the rather similar TEM-derived Co^0 particle sizes and size distributions in both Co-Ru/Ti-R and Co-Ru/Ti-A catalysts (Fig. 7, Table 4) discard any significant contribution of this factor to the observed catalytic performance. Other authors also found a constant TOF of ca. 0.20 s^{-1} for Co/TiO_2 samples with different TiO_2 phase compositions, which is about twice the TOF obtained in the present work albeit at a higher reaction temperature (230 °C) [18].

The apparently similar TOFs obtained in this work for the anatase- and rutile-supported catalysts contrasts with the significantly distinct electronic character of the Co^0 sites exposed on surface of the H_2 reduced catalysts according to the previous IR-CO results (Fig. 9). Indeed, a different reactivity towards CO dissociation for Co^0 sites in defects such as corners, edges, and steps and in terraces of the nanoparticles has been postulated on the basis of DFT calculations [65, 66]. However, metal cobalt nanoparticles are known to experience surface reconstruction under syngas atmosphere at typical FTS temperatures that produces a change in their surface topology and hence in the type of exposed Co^0 sites [22, 62]. Therefore, we performed additional *in situ* IR experiments in order to elucidate the nature of the surface Co^0 sites in the two catalysts when exposed to syngas conversion conditions at the FTS temperature of 220 °C. The results are discussed in the following section.

3.3.2. In situ IR-CO under syngas reaction conditions

The IR-CO spectra at CO saturation coverage after H_2 reduction and after reaction with syngas at 220 °C for 4 h are shown in Fig. 10. A shift of the main Co-carbonyl band towards lower frequencies is observed for both catalysts, which clearly evidences surface reconstruction of the Co^0 nanoparticles towards more open planes when exposed to syngas at FTS conditions [22]. Interestingly, the amount of surface Co^0 sites titrated by CO for the anatase-based catalyst substantially increased after syngas reaction with respect to the as-reduced state (Fig. 10a,b). This fact reveals that the significant SMSI effect experienced by this catalyst during the reduction process was at least partially reversed during reaction with syngas. A certain recovery of the normal (non-SMSI) state has also been reported for other metals like Pt and Rh supported on TiO_2 when exposed to a CO/H_2 mixture at 275 °C [67]. According to these authors, the water produced during the syngas conversion was responsible for the observed partial reversibility of the SMSI effect [67]. As a consequence of the dynamic character of the SMSI effect, the surface state of the supported Co^0 nanoparticles under syngas conversion conditions turns similar for the two Co-Ru/TiO_2 catalysts, as indicated by the alike frequency of their main CO-Co^0 IR band (2041 and 2050 cm^{-1} for the anatase- and rutile-supported catalysts, Fig. 10b,d). It should be noted that the anatase and rutile phases remained 100% pure without appreciable variation in the mean

TiO$_2$ crystallite size in the corresponding catalysts after being exposed to FTS reaction at high pressure conditions (see Fig. S3 and Table S1 in Supplementary Material).

The above *at work* IR results might thus account for the comparable TOFs obtained for the two catalysts (Table 5). However, the fact that the SMSI effect was partially reversed for the anatase-based catalyst implies a higher amount of active surface Co^0 sites under *working* conditions compared to that measured for the as-reduced sample and, consequently, a lower TOF than that calculated from H$_2$ chemisorption. Taking this into account, a dependence of TOF on the TiO$_2$ crystal phase may be inferred, although additional work is advised to reach a definitive conclusion on this issue.

3.3.3. Product distribution

As for the product distribution (Table 6), both catalysts show low selectivity to CO$_2$ (< 1 %C) as expected from the well known low activity of Co^0 for catalyzing the competing water-gas-shift reaction (WGSR). The distribution of hydrocarbons indicate, at similar CO conversion (10 $\pm$ 1%), a higher selectivity to the desired C$_{5+}$ liquid fraction (79.1%) and lower selectivity to methane (9.5%) for Co-Ru/Ti-R in comparison to Co-Ru/Ti-A (S$_{C1}$= 14.9%, S$_{C5+}$= 62.0%).

Table 6

Based on surface science studies, it has been proposed that activation of CO and monomer (CH$_x$) formation is favored on under-coordinated Co^0 sites at step edges while chain growth requires rather large ensembles of Co^0 atoms in close-packed terraces of cobalt crystallites [68]. Considering this, the SMSI decoration effect is expected to reduce the size of the surface ensembles at the terraces and, consequently, to disfavor chain growth processes. Thus, the more pronounced SMSI effect found for the anatase-based catalyst might account, in principle, for its lower C$_{5+}$ selectivity in comparison to the rutile-based one. However, our *at work* IR-CO results clearly evidenced the partial reversibility of the SMSI effect by which most of the decorated Co^0 sites in CoRu/Ti-A were uncovered under syngas reaction conditions. In turn, the IR-CO results also indicated an analogous electronic nature of the surface Co^0 atoms (i.e. similar frequency for the CO-Co^0 bands) in both catalysts under

reaction conditions. Therefore, a clear impact of the SMSI effect on product selectivity, although not discarded, cannot be definitively concluded from our study.

On the other hand, mass transfer limitations are known to significantly impact the selectivity of Co catalysts under realistic FTS conditions where the pores are filled with liquid hydrocarbons. This effect is particularly relevant for catalysts with relatively small pores and pellet sizes typically applied for fixed bed reactor operations [69]. Under this situation, the H_2/CO ratio around the Co particles located within the pores increases with respect to that in the gas phase favoring the hydrogenation of intermediates and shifting the product distribution towards lighter hydrocarbons. As observed in Table 6, the olefin-to-paraffin (O/P) weight ratio in the analyzed C_2-C_4 fraction is 1.6 for Co-Ru/Ti-A and 2.0 for Co-Ru/Ti-R. Thus, the more paraffinic nature of the hydrocarbons in the anatase-based catalyst points towards a higher extent of hydrogenation of the primary α-olefins that aligns with a more impeded diffusion of CO in this catalyst than in the rutile-based sample. Accordingly, the higher C_{5+} selectivity of the Co-Ru/Ti-R sample is likely ascribed to an enhanced mass transfer rate for CO in the larger pores of the rutile TiO_2 support. Besides secondary hydrogenation, the primary α-olefins may also undergo double-bond and skeletal isomerizations during FTS. Although the relevance of α-olefin re-adsorption on the ultimate product selectivity remains controversial, α-olefin isomerization reactions would prevent their participation in chain growth processes and, hence, lower the selectivity to long-chain hydrocarbons. In our case, the analysis of the C_4 fraction revealed the absence of isobutane and isobutene products, indicating that branching isomerization did not occur on the Co-Ru/TiO_2 catalysts at the investigated conditions. Differently, the formation of *cis*- and *trans*-2-butene was observed on both catalysts, though in different extents. Hence, 2-butene/1-butene ratios of 0.20 and 0.16 were obtained for, respectively, the anatase- and rutile-based catalysts (Table 6), indicating that olefin double-bond migration is more favored on the former polymorph. Recently, by using monolayer-type model Co catalysts we have demonstrated the significance of the surface acid-base character of the oxide support in determining the extent of secondary α-olefin reactions during FTS and, consequently, the final product selectivity [5]. Despite large variations in surface acidity are not expected for the different TiO_2 polymorphs, anatase has been experimentally proved to contain stronger surface Lewis acid sites (associated to coordinatively unsaturated Ti^{4+} ions) than rutile [70, 71]. Therefore, it is sensible that the higher surface acidity of TiO_2 anatase accounts for the

favored α-olefin double-bond isomerization observed for Co-Ru/Ti-A, and that this may contribute to the lower C_{5+} selectivity displayed by this catalyst (Table 6).

4. Conclusions

The following main conclusions can be withdrawn from the present study:

1) Ru-promoted Co catalysts (10 wt% Co-0.5 wt% Ru nominal loadings) supported on 100% pure anatase (CoRu/Ti-A) and rutile (CoRu/Ti-R) TiO_2 polymorphs experienced the SMSI decoration effect during the H_2 reduction treatment at 400 °C performed prior to catalysis.

2) The extent of the SMSI effect was much more pronounced for CoRu/Ti-A leading to much lower H_2 and CO chemisorption capacities for the supported Co^0 nanoparticles (NPs) compared to CoRu/Ti-R.

3) The higher extent of the SMSI effect in CoRu/Ti-A resulted in a decreased activity (by about 50%) for Fischer-Tropsch synthesis (FTS) with respect to CoRu/Ti-R in terms of both CO conversion and cobalt-time-yield (CTY) at 220 °C, 2.0 MPa, and H_2/CO= 2.

4) Conversely, the two catalysts showed comparable TOFs (based on H_2 chemisorption) at both initial (9-10·10^{-2} s^{-1}) and pseudo-steady state (ca. 6.5·10^{-2} s^{-1}) conditions.

5) A similar extent of surface reconstruction (towards more defected planes) leading to an alike electronic nature of the accessible Co^0 sites for both the anatase- and rutile-supported catalysts was found by *in situ* IR-CO spectroscopy after exposing the reduced samples to syngas flow at 220 °C (0.1 MPa) for 4 h.

6) The SMSI effect was seen to be partially reversible under syngas reaction conditions significantly increasing the amount of surface Co^0 sites available for reaction in the anatase-based catalyst. This observation questions TOFs calculated from H_2 chemisorption in TiO_2-supported catalysts and points towards a dependence of TOF on the TiO_2 polymorph, advising for further studies to definitively elucidate this issue.

7) At constant CO conversion the rutile-based catalyst displayed higher C_{5+} selectivity than that based on anatase, which was ascribed to an enhanced mass transfer (due to its larger pores) as well as to a lower surface acidity (inhibiting α-olefins double bond migration) of rutile relative to anatase. A clear impact of the SMSI effect on product selectivity, although not discarded, could not be definitively concluded from our work.

References

[1] A.Y. Khodakov, W. Chu, P. Fongarland, Chem. Rev. 107 (2007) 1692-1744.

[2] M.E. Dry, J. Chem. Technol. Biotechnol. 77 (2002) 43-50.

[3] R. Oukaci, A.H. Singleton, J.G. Goodwin Jr., Appl. Catal. A: Gen. 186 (1999) 129-144.

[4] A.Y. Khodakov, Catal. Today 144 (2009) 251-257.

[5] G. Prieto, M.I.S. De Mello, P. Concepción, R. Murciano, S.B.C. Pergher, A. Martínez, ACS Catal. 5 (2015) 3323-3335.

[6] E. Iglesia, S.L. Soled, R.A. Fiato, J. Catal. 137 (1992) 212-224.

[7] G. Prieto, P. Concepción, R. Murciano, A. Martínez, J. Catal. 302 (2013) 37-48.

[8] R.C. Reuel, C.H. Bartholomew, J. Catal. 85 (1984) 78-88.

[9] E. Iglesia, S.L. Soled, R.A. Fiato, G.H. Via, J. Catal. 143 (1993) 345-368.

[10] S.J. Tauster, S.C. Fung, R.L. Garten, J. Am. Chem. Soc. 100 (1978) 170-175.

[11] J. Van De Loosdrecht, A.M. Van Der Kraan, A.J. Van Dillen, J.W. Geus, J. Catal. 170 (1997) 217-226.

[12] A. Dandekar, M.A. Vannice, J. Catal. 183 (1999) 344-354.

[13] J.C. Colmenares, A. Magdziarz, M.A. Aramendia, A. Marinas, J.M. Marinas, F.J. Urbano, J.A. Navio, Catal, Commun. 16 (2011) 1-6.

[14] S.J. Tauster, S.C. Fung, R.T.K. Baker, J.A. Horsley, Science 211 (1981) 1121-1125.

[15] V.A. De La Peña O'Shea, M. Consuelo Álvarez Galván, A.E. Platero Prats, J.M. Campos-Martin, J.L.G. Fierro, Chem. Commun. 47 (2011) 7131-7133.

[16] B. Jongsomjit, T. Wongsalee, P. Praserthdam, Catal. Commun. 6 (2005) 705-710.

[17] B. Jongsomjit, C. Sakdamnuson, P. Praserthdam, Mater. Chem. Phys. 89 (2005) 395-401.

[18] K. Shimura, T. Miyazawa, T. Hanaoka, S. Hirata, Appl. Catal. A: Gen. 460-461 (2013) 8-14.

[19] K. Shimura, T. Miyazawa, T. Hanaoka, S. Hirata, Catal. Today, 232 (2014) 2-10.

[20] M. Andersson, A. Kiselev, L. Österlund, A.E.C. Palmqvist, J. Phys. Chem. C 111 (2007) 6789-6797.

[21] R.C. Reuel, C.H. Bartholomew, J. Catal. 85 (1984) 63-77.

[22] G. Prieto, A. Martínez, P. Concepción, R. Moreno-Tost, J. Catal. 266 (2009) 129-144.

[23] M. Wu, J. Long, A. Huang, Y. Luo, S. Feng, R. Xu, Langmuir 15 (1999) 8822-8825.

[24] D. Zhang, L. Qi, J. Ma, H. Cheng, J. Mater. Chem. 12 (2002) 3677-3680.

[25] M. Wu, G. Lin, D. Chen, G. Wang, D. He, S. Feng, R. Xu, Chem. Mater. 14 (2002) 1974-1980.

[26] C. Sanchez, J. Livage, M. Henry, F. Babonneau, J. Non-Crystal. Solids 100 (1988) 65-76.

[27] M. Thommes, K. Kaneko, A.V. Neimark, J.P. Olivier, F. Rodriguez-Reinoso, J. Rouquerol, K.S.W. Sing, Pure Appl. Chem. 87 (2015) 1051-1069.

[28] M. Andersson, L. Österlund, S. Ljungström, A. Palmqvist, J. Phys. Chem. B 106 (2002) 10674-10679.

[29] Q. Chen, C. Chen, H. Ji, W. Ma, J. Zhao, RSC Adv. 3 (2013) 17559-17566.

[30] Y. Wang, L. Zhang, K. Deng, X. Chen, Z. Zou, J. Phys. Chem. C 111 (2007) 2709-2714.

[31] T. Lopez, L. Herrera, R. Gomez, W. Zou, K. Robinson, R.D. Gonzalez, J. Catal. 136 (1992) 621-625.

[32] J.S. Girardon, E. Quinet, A. Griboval-Constant, P.A. Chernavskii, L. Gengembre, A.Y. Khodakov, J. Catal. 248 (2007) 143-157.

[33] A. Martínez, G. Prieto, J. Rollán, J. Catal. 263 (2009) 292-305.

[34] B. Jongsomjit, C. Sakdamnuson, J.G. Goodwin Jr, P. Praserthdam, Catal. Lett. 94 (2004) 209-215.

[35] I. Florea, Y. Liu, O. Ersen, C. Meny, C. Pham-Huu, ChemCatChem 5 (2013) 2610-2620.

[36] D. Schanke, S. Vada, E.A. Blekkan, A.M. Hilmen, A. Hoff, A. Holmen, J. Catal. 156 (1995) 85-95.

[37] Y. Li, Y. Fan, H. Yang, B. Xu, L. Feng, M. Yang, Y. Chen, Chem. Phys. Lett. 372 (2003) 160-165.

[38] Q. Cai, J. Li, Catal. Commun. 9 (2008) 2003-2006.

[39] K.M. Cook, S. Poudyal, J.T. Miller, C.H. Bartholomew, W.C. Hecker, Appl. Catal. A: Gen. 449 (2012) 69-80.

[40] T.O. Eschemann, J. Oenema, K.P. De Jong, Catal. Today 261 (2016) 60-66.

[41] G. Jacobs, T.K. Das, Y. Zhang, J. Li, G. Racoillet, B.H. Davis, App. Catal. A: Gen. 233 (2002) 263-281.

[42] P. Li, J. Liu, N. Nag, P.A. Crozier, App. Catal. A: Gen. 307 (2006) 212-221.

[43] J.Y. Park, Y.J. Lee, P.R. Karandikar, K.W. Jun, J.W. Bae, K.S. Ha, J. Mol. Catal. A: Chem. 344 (2011) 153-160.

[44] G. Melaet, W.T. Ralston, C.S. Li, S. Alayoglu, K. An, N. Musselwhite, B. Kalkan, G.A. Somorjai, J. Am. Chem. Soc. 136 (2014) 2260-2263.

[45] A.M. Saib, D.J. Moodley, I.M. Ciobîc, M.M. Hauman, B.H. Sigwebela, C.J. Weststrate, J.W. Niemantsverdriet, J. Van De Loosdrecht, Catal. Today 154 (2010) 271-282.

[46] K.H. Cats, I.D. Gonzalez-Jimenez, Y. Liu, J. Nelson, D. Van Campen, F. Meirer, A.M.J. Van Der Eerden, F.M.F. De Groot, J.C. Andrews, B.M. Weckhuysen, Chem. Commun. 49 (2013) 4622-4624.

[47] S. Storsæter, B. Tøtdal, J.C. Walmsley, B.S. Tanem, A. Holmen, J. Catal. 236 (2005) 139-152.

[48] Ø. Borg, S. Eri, E.A. Blekkan, S. Storsæter, H. Wigum, E. Rytter, A. Holmen, J. Catal. 248 (2007) 89-100.

[49] A.Y. Khodakov, A. Griboval-Constant, R. Bechara, V.L. Zholobenko, J. Catal. 206 (2002) 230-241.

[50] Y. Liu, K. Fang, J. Chen, Y. Sun, Green Chem., 9 (2007) 611-615.

[51] D. Song, J. Li, J. Mol. Catal. A: Chem. 247 (2006) 206-212.

[52] H. Xiong, Y. Zhang, K. Liew, J. Li, J. Mol. Catal. A: Chem. 295 (2008) 68-76.

[53] Y. Li, B. Xu, Y. Fan, N. Feng, A. Qiu, J.M.J. He, H. Yang, Y. Chen, J. Mol. Catal. A: Chem. 216 (2004) 107-114.

[54] D.G. Castner, P.R. Watson, I.Y. Chan, J. Phys. Chem. 93 (1989) 3188-3194.

[55] I. Jirka, J. Phys. Chem. B 105 (2001) 1140-1148.

[56] J.G. Dillard, M.H. Koppelman, J. Coll. Interf. Sci. 87 (1982) 46-55.

[57] Z. Zsoldos, L. Guczi, J. Phys. Chem. 96 (1992) 9393-9400.

[58] D. Song, J. Li, Q. Cai, J. Phys. Chem. C 111 (2007) 18970-18979.

[59] P. Concepción, A. Corma, J. Silvestre-Albero, V. Franco, J.Y. Chane-Ching, J. Am. Chem. Soc. 126 (2004) 5523-5532.

[60] T.O. Eschemann, K.P. De Jong, ACS Catal. 5 (2015) 3181-3188.

[61] T.O. Eschemann, J.H. Bitter, K.P. De Jong, Catal. Today 228 (2014) 89-95.

[62] G.L. Bezemer, J.H. Bitter, H.P.C.E. Kuipers, H. Oosterbeek, J.E. Holewijn, X. Xu, F. Kapteijn, A.J. Van Diilen, K.P. De Jong, J. Am. Chem. Soc. 128 (2006) 3956-3964.

[63] J.A. Delgado, C. Claver, S. Castillón, D. Curulla-Ferré, V.V. Ordomsky, C. Godard, Appl. Catal. A: Gen. 513 (2016) 39-46.

[64] Y. Liu, I. Florea, O. Ersen, C. Pham-Huu, C. Meny, Chem. Commun. 51 (2015) 145-148.

[65] S. Shetty, A.P.J. Jansen, R.A. Van Santen, J. Am. Chem. Soc. 131 (2009) 12874-12875.

[66] R.A. Van Santen, M.M. Ghouri, S. Shetty, E.M.H. Hensen, Catal. Sci. and Technol. 1 (2011) 891-911.

[67] J.B.F. Anderson, R. Burch, J.A. Cairns, Appl. Catal. 21 (1986) 179-185.

[68] C.J. Weststrate, P. van Helden, J.W. Niemantsverdriet, Catal. Today, 2016, doi: 10.1016/j.cattod.2016.04.004.

[69] E. Iglesia, Appl. Catal. A: Gen. 161 (1997) 59-78.

[70] H. Li, M. Vrinat, G. Berhault, D. Li, H. Nie, P. Afanasiev, Mater. Res. Bull. 48 (2013) 3374-3382.

[71] M. Addamo, M. Del Arco, M. Bellardita, D. Carriazo, A. Di Paola, E. García-López, G. Marcì, C. Martín, L. Palmisano, V. Rives, Res. Chem. Interm. 33 (2007) 465-479.

Table 1. Nomenclature and conditions employed for the synthesis of pure TiO_2 anatase and rutile phases.

Support	Acid	Temperature (°C)	Time (h)	w = $[H_2O]/[Triton]$ (mol/mol)	h = $[H_2O]/[Ti]$ (mol/mol)
Ti-A	CH_3COOH	120	5	19.4	33.8
Ti-R	HCl	40	24	15.0	18.8

Table 2. Main physicochemical properties of TiO_2 supports.

Support	BET area (m^2/g)	TPV[a] (cm^3/g)	APD[b] (nm)	d(TiO$_2$)[c] (nm)
Ti-A	164	0.30	6.4	9.5
Ti-R	59	0.17	7.3	13.6

[a] TPV= Total pore volume. [b] APD= Average pore diameter (BJH). [c] Mean TiO$_2$ crystallite size.

Table 3. Chemical composition and textural properties of the calcined CoRu/TiO$_2$ catalysts.

Catalyst	Metal content		BET area		TPV[a]		APD[b]
	wt% Co	wt% Ru	(m^2/g$_{cat}$)	(m^2/g$_{TiO2}$)	(cm^3/ g$_{cat}$)	(cm^3/g$_{TiO2}$)	(nm)
Co-Ru/Ti-A	11.7	0.3	126	151	0.23	0.27	6.1
Co-Ru/Ti-R	11.1	0.4	42	50	0.14	0.16	8.4

[a] TPV= Total pore volume. [b] APD= Average pore diameter (BJH).

Table 4. Properties of cobalt in the CoRu/TiO$_2$ catalysts.

Catalyst	DR[a] (%)	H$_2$ uptake (μmol/g$_{cat}$)	Co^0 particle size (nm)		Atomic (Co/Ti)$_{surf}$ ratio	
			d(Co^0)$_{H2}$	d(Co^0)$_{TEM}$	Calcined	H$_2$-reduced
Co-Ru/Ti-A	93	13.8	64.7	5.2	0.08	0.32
Co-Ru/Ti-R	89	27.3	29.5	6.0	0.24	0.30

[a] Percentage degree of cobalt reduction upon treatment in pure H$_2$ at 400 °C for 10 h.
[b] Atomic Co/Ti surface ratio in calcined and as-reduced catalysts determined by XPS.

Table 5. Initial and *pseudo*-steady state activities (SS) of Co-Ru/TiO$_2$ catalysts for Fischer-Tropsch synthesis (FTS). Reaction conditions: T= 220 °C, P= 2.0 MPa, H$_2$/CO= 2 mol/mol. Initial activities were obtained by extrapolating the CO conversion-TOS curves at TOS= 0 at constant GHSV of 11.7 L$_{syngas}$/(g$_{cat}$·h), while SS activities were averaged for the next 8 h of reaction after adjusting the GHSV for each catalyst so as to obtain a CO conversion of ~ 10%.

Catalyst	CO conversion (%)		CTY·10^3 (mol$_{CO}$/g$_{Co}$/h)^a		TOF·10^2 (s^{-1})^b	
	Initial	SS	Initial	SS	Initial	SS
Co-Ru/Ti-A	6.6	8.8	89.3	53.2	10.5	6.3
Co-Ru/Ti-R	11.0	10.9	156.8	113.5	8.9	6.5

^{a} CTY= cobalt-time-yield (activity per total mass of cobalt).

^{b} TOF= turnover frequency (activity per surface Co^0 sites as measured by H$_2$ chemisorption).

Table 6. Product selectivities obtained in the steady state over Co-Ru/TiO$_2$ catalysts at similar CO conversion (10 $\pm$ 1%). Reaction conditions: T= 220 °C, P= 2.0 MPa, H$_2$/CO= 2 mol/mol, GHSV= 5.2 (for Co-Ru/Ti-A) and 8.5 (for Co-Ru/Ti-R) L$_{syngas}$/g$_{cat}$/h.

Catalyst	S$_{CO2}$ (%C)	Hydrocarbons (%C)			O/P ratio[a] (wt/wt)	2-C$_4^=$/1-C$_4^=$ ratio
		C$_1$	C$_2$-C$_4$	C$_{5+}$		
Co-Ru/Ti-A	1.0	14.9	23.1	62.0	1.6	0.20
Co-Ru/Ti-R	0.6	9.5	11.4	79.1	2.0	0.16

[a] Olefin-to-paraffin weight ratio for the C$_2$-C$_4$ hydrocarbon fraction.

Figures

Figure 1. X-ray diffraction patterns of calcined TiO_2 supports. Diffraction lines for pure anatase (JCPDS 00-021-1272) and rutile (JCPDS 00-021-1276) phases are also shown as reference.
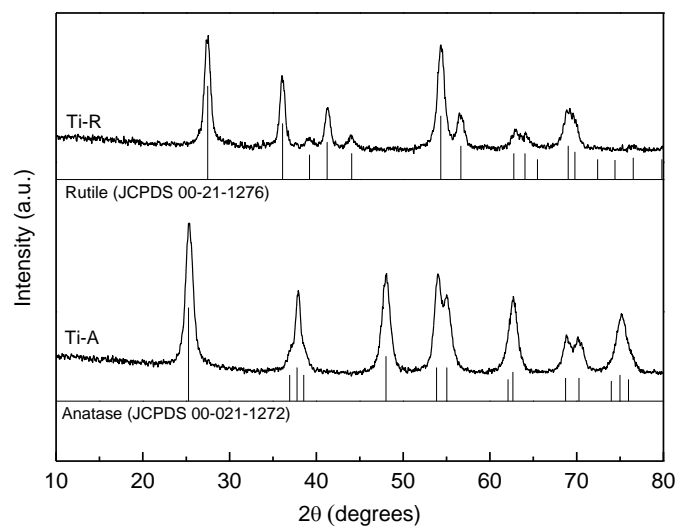
Figure 2. N_2 adsorption isotherms (A) and BJH-derived pore size distributions (B) for the calcined anatase (Ti-A) and rutile (Ti-R) samples.
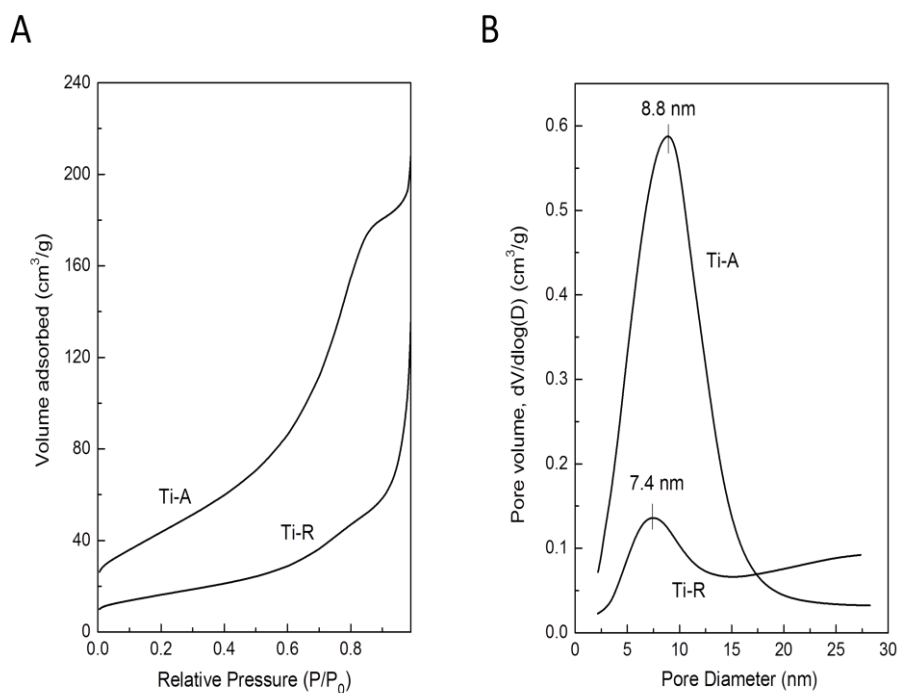
Figure 3. FESEM images for: a) anatase (Ti-A) and b) rutile (Ti-R) TiO$_2$ samples.
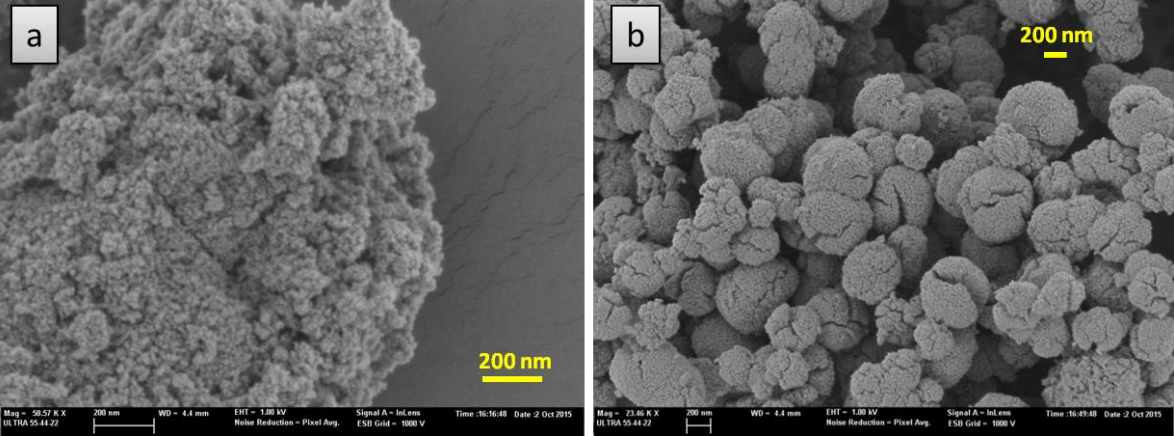
Figure 4. X-ray diffraction patterns of calcined Co-Ru/Ti-A and Co-Ru/Ti-R catalysts.
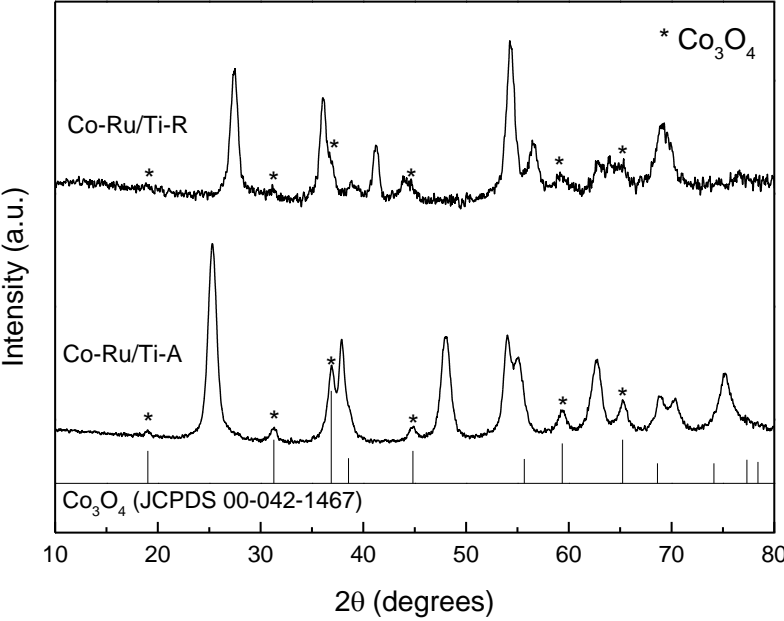
Figure 5. N$_2$ adsorption isotherms (A) and BJH-derived pore size distributions (B) for the calcined Co-Ru/Ti-A and Co-Ru/Ti-R catalysts.
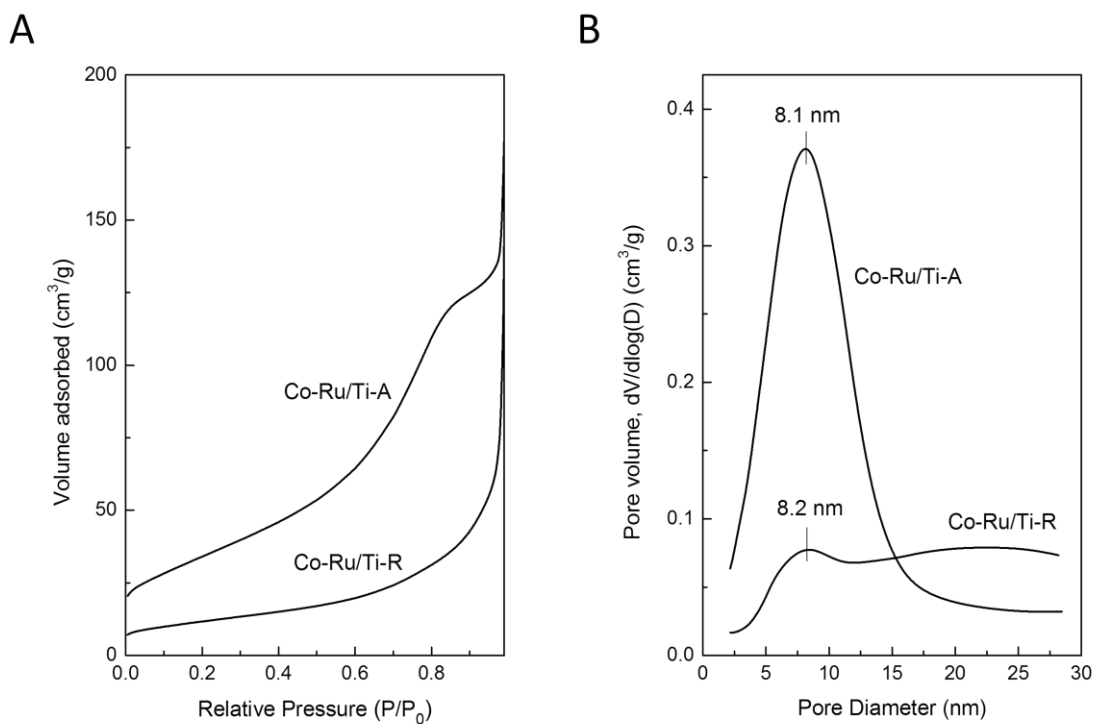
Figure 6. H$_2$-TPR profiles for the Co-Ru/TiO$_2$ catalysts.
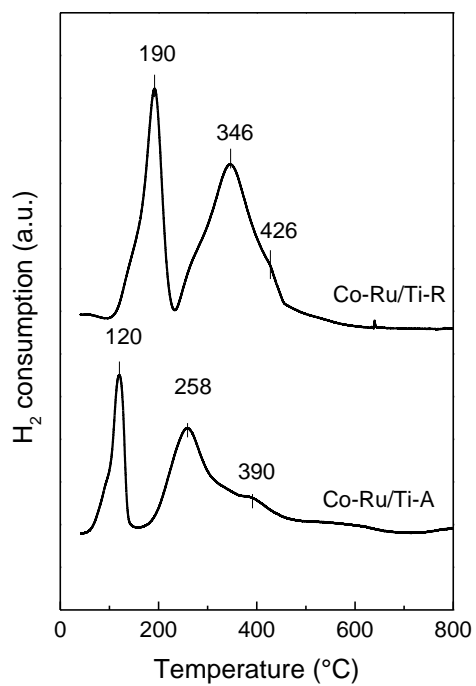
Figure 7. Representative HAADF-STEM images (A, C) and the derived metallic cobalt particle size histograms (B, D) for the H_2-reduced Co-Ru/Ti-A (A, B) and Co-Ru/Ti-R (C, D) catalysts. Co^0 particle sizes have been corrected by a 3 nm thick CoO outlayer.
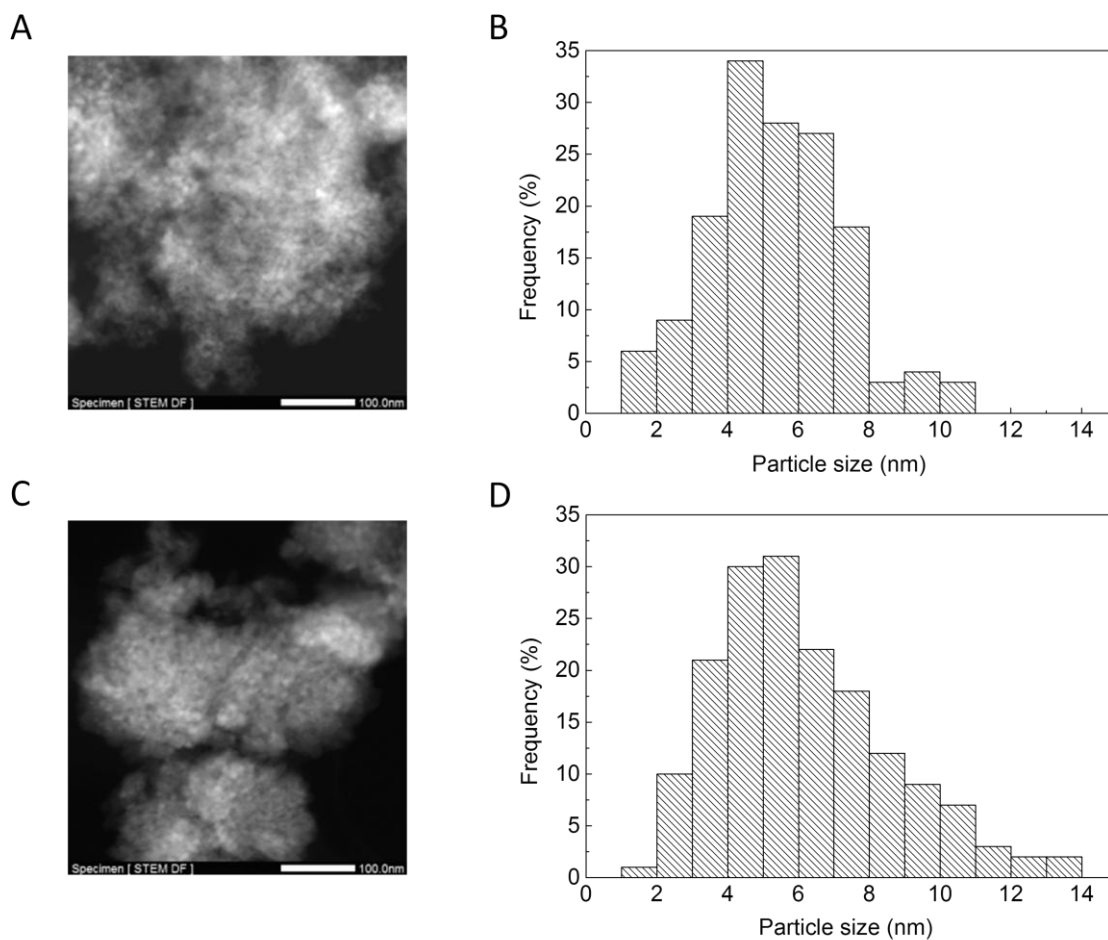
Figure 8. Co2p$_{3/2}$ XPS core level spectra for calcined (A) and H$_2$-reduced (B) catalysts: a) Co-Ru/Ti-A, b) Co-Ru/Ti-R. Sat* is the satellite peak associated to Co^{2+}.
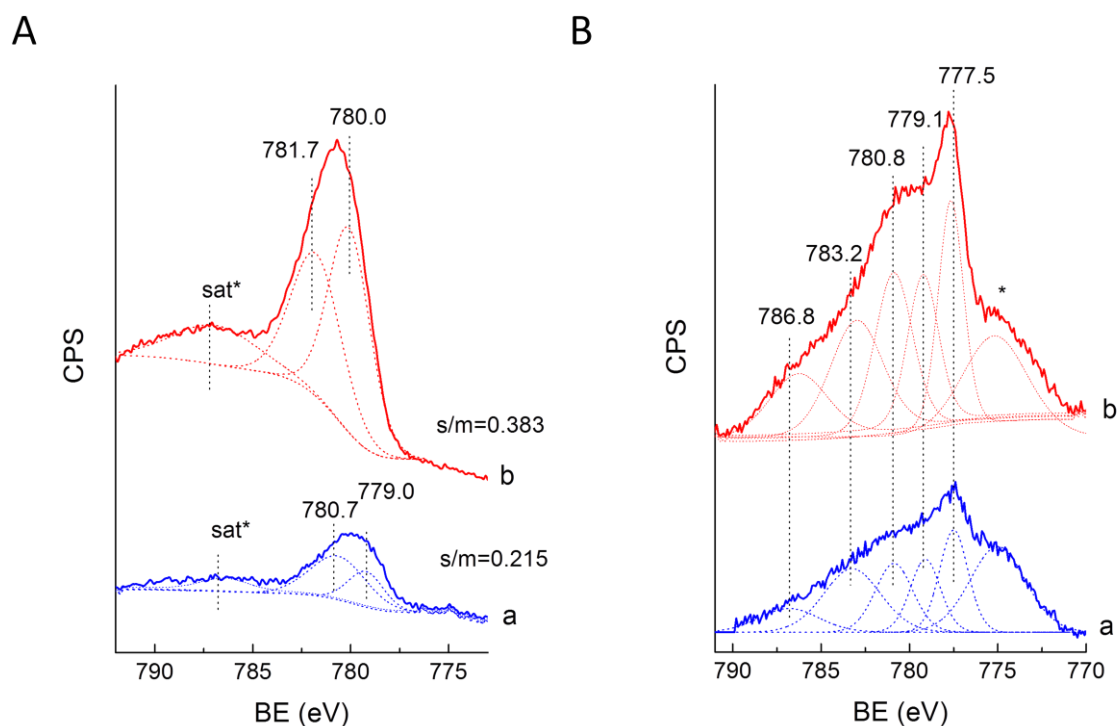
Figure 9. IR-CO spectra at r.t. and increasing CO doses (1.9 $\rightarrow$ 30 mbar) for H$_2$-reduced Co-Ru/Ti-R (A) and Co-Ru/Ti-A (B) samples.
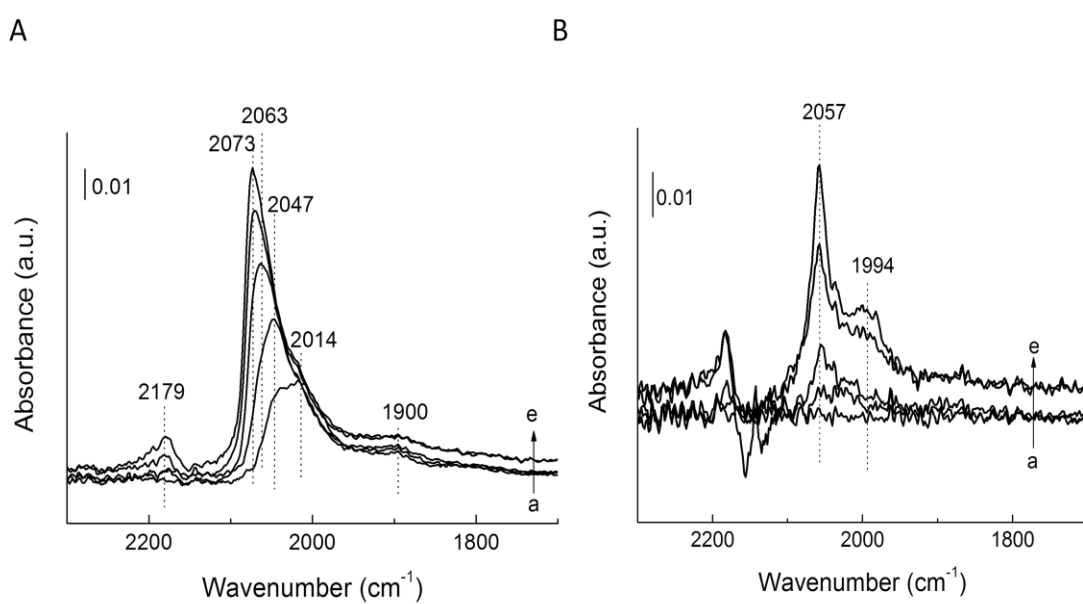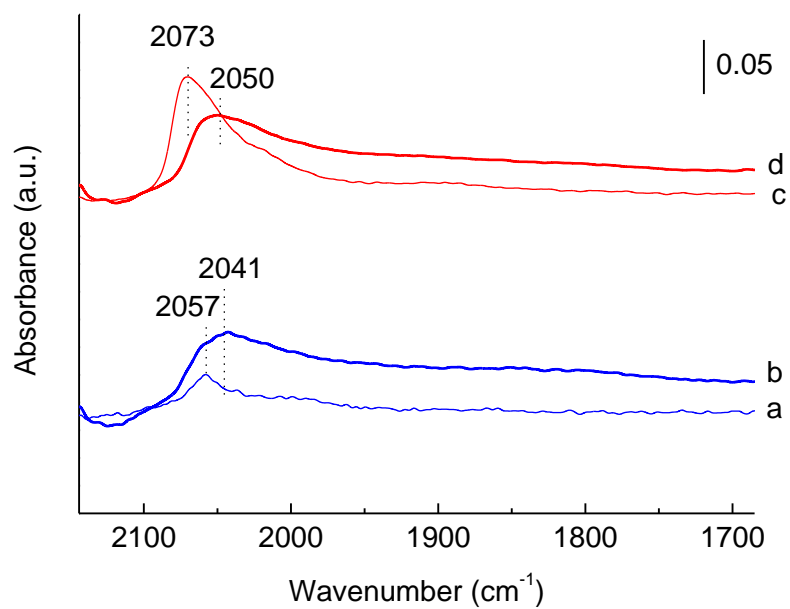
Figure 10. IR-CO spectra at saturation CO coverage recorded after H_2 reduction (a,c) and after *in situ* reaction with syngas at 220ºC for 4 h (b,d) for Co-Ru/Ti-A (a,b) and Co-Ru/Ti-R (c,d) catalysts.

Supplementary Material

for

TiO$_2$ polymorph dependent SMSI effect in Co-Ru/TiO$_2$ catalysts and its relevance to Fischer-Tropsch synthesis

Francine Bertella [a,b], Patricia Concepción [a], Agustín Martínez [a,*]

Instituto de Tecnología Química, CSIC- UPV, Avda. de los Naranjos s/n, 46022

Valencia, Spain

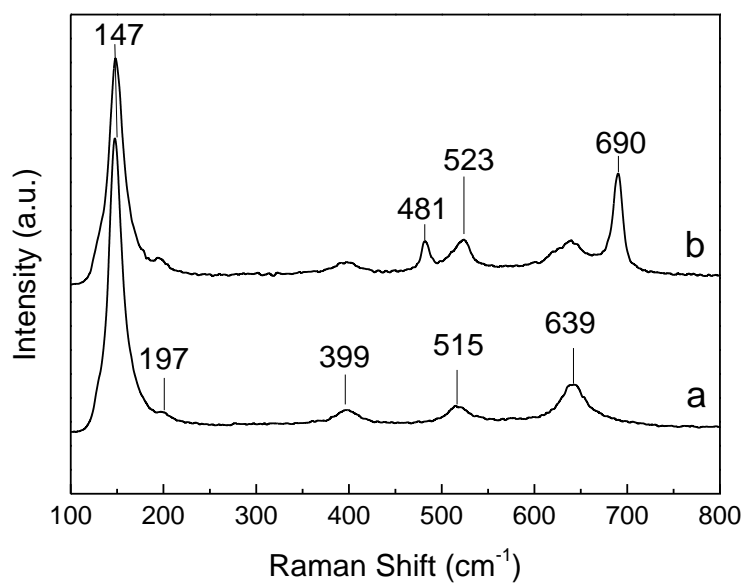# RAMAN SPECTROSCOPY OF CALCINED CoRu/TiO₂ CATALYSTS

Experimental

Raman spectra of calcined samples were acquired in a Renishaw in Via Raman spectrometer equipped with a Leica DMLM microscope. A 50x objective of 1 mm optical length was used to focus the depolarized laser beam onto a 3–5 μm spot on the sample surface and collect the backscattered light. As an excitation source a 514 nm HPNIR diode laser was used and the laser power at the sample was 25 mW. The Raman scattering was collected in a static-scan mode in the 100–800 cm^{-1} spectral region with resolution > 4 cm^{-1}.

Discussion of Raman results

The Raman spectra for the calcined CoRu/Ti-A and CoRu/Ti-R catalysts are presented, along with those of the respective TiO₂ supports, in Figure S1.
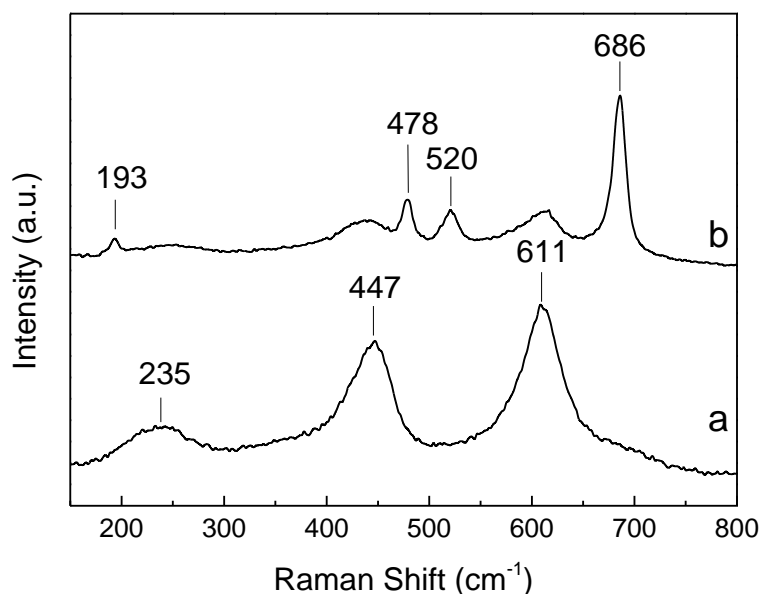
B

Figure S1. Raman spectra of the TiO$_2$ supports and corresponding CoRu/TiO$_2$ catalysts: A) Ti-A (a) and CoRu/Ti-A (b), and B) Ti-R (a) and CoRu/Ti-R (b).

The calcined CoRu/Ti-A sample (Fig. S1A-b) displays Raman bands at 147, 197, 399, 515, and 639 cm^{-1} characteristic of the anatase TiO$_2$ polymorph (Fig. S1A-a) [1], along with active bands at 481, 523, and 690 cm^{-1} assigned to the spinel Co$_3$O$_4$ phase [2]. As for CoRu/Ti-R (Fig. S1B-b), the characteristic Raman bands of the rutile phase at 235, 447, and 611 cm^{-1} (Fig. S1B-a) [1] as well as those of Co$_3$O$_4$ (481, 523, and 690 cm^{-1}) are clearly identified. No Raman bands related to the CoTiO$_3$ mixed oxide, for which the strongest and most representative Raman active band peaks at 696 cm^{-1} [3], are evidenced in none of the calcined catalysts.

References

[1] J. Zhang, M. Li, Z. Feng, J. Chen, C. Li, J. Phys. Chem. B 110 (2006) 927.

[2] V.G. Hadjiev, M.N. Iliev, I. V Vergilov, J. Phys. C: Solid State Phys. 21 (1988) L199.

[3] M.A. Ehsan, R. Naeem, H. Khaledi, M. Sohail, A. Hakeem Saeed, M. Mazhar, Dalton Trans. 45 (2016) 10222.

CRYSTALLINE PHASES IN THE H$_2$-REDUCED CATALYSTS

Experimental

In situ H$_2$-XRD measurements were performed to assess the crystalline phases present in the as-reduced catalysts. The measurements were performed in a Panalytical X'Pert PRO diffractometer using monochromatized CuK$_\alpha$ radiation and operated at 45 kV and 40 mA. The samples were loaded in a XRK-900 Anton Paar cell and flushed with a gas stream comprising 5 vol% H$_2$ diluted in N$_2$. In these experiments, the X-ray diffractograms were first recorded at 30 °C (corresponding to the calcined state of the catalysts) and then the temperature was raised to 400 °C under the diluted H$_2$ flow. Once the reduction temperature was reached, patterns were recorded every hour until a constant diffractogram was observed (typically after 7 h).

XRD patterns of as-reduced catalysts

The XRD patterns of the catalysts after in situ reduction in H$_2$ at 400 °C for 7 h are shown in Figure S2. A clear identification of the crystalline cobalt phases present in the reduced catalysts is not feasible due to overlapping with the intense TiO$_2$ peaks. Nevertheless, weak peaks at 44.2° and 47.5° (2θ) corresponding to the most intense reflections of, respectively, fcc-Co^0 (JCPDS 00-15-0806) and hcp-Co^0 (JCPDS 00-005-0727) crystalline phases are evidenced in both catalysts. Moreover, the reflections associated to the spinel Co$_3$O$_4$ oxide present in the calcined materials (Fig. 4) are not longer evidenced in the H$_2$-reduced samples, signing for a high degree of Co$_3$O$_4 \rightarrow$ Co^0 reduction, in agreement with the obtained H$_2$-TPR profiles. In turn, no crystalline phases related to Co-Ti alloys or mixed oxides are perceived for any of the as-reduced catalysts.
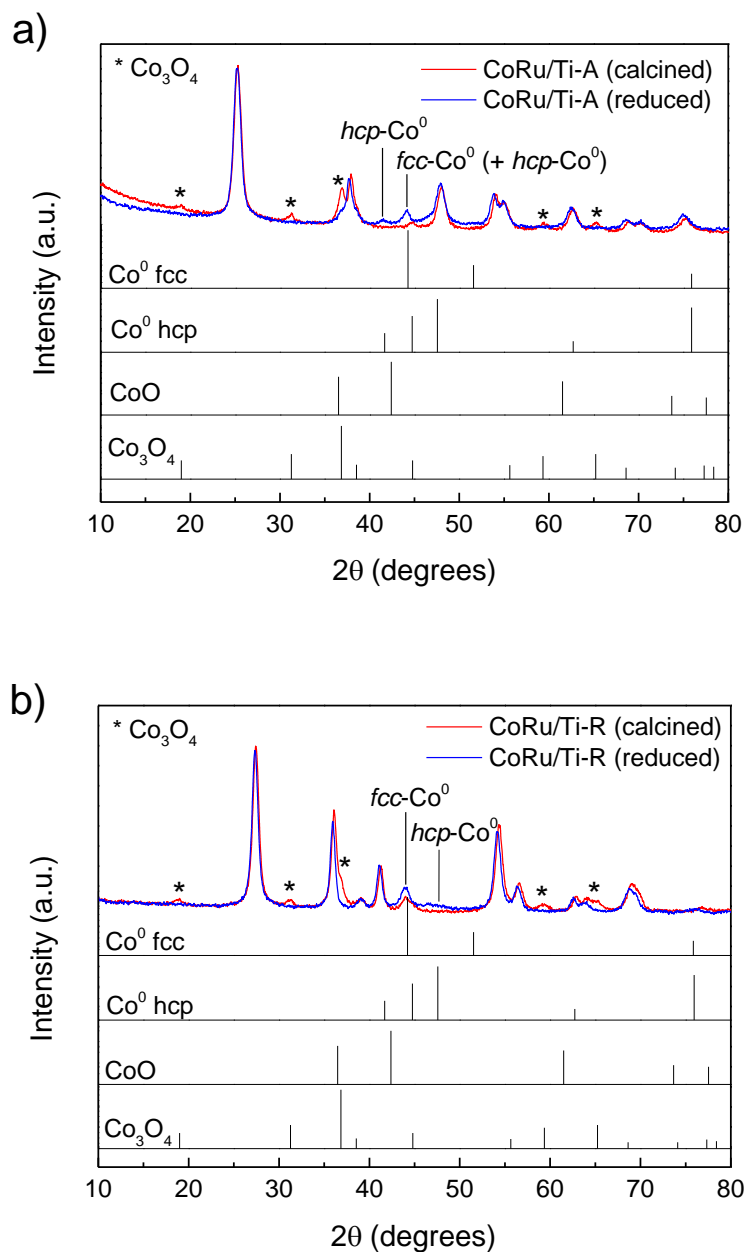
Figure S2. XRD patterns recorded after in situ reduction for 7 h in diluted H_2 flow (5 vol% H_2 in N_2) at 400 °C for CoRu/Ti-A (a) and CoRu/Ti-R (b) catalysts. For each catalyst, the XRD pattern recorded at 30 °C is also included for comparative purposes as representative of the as-calcined state. The patterns of reference cobalt compounds are shown for an easier identification of the crystalline phases.
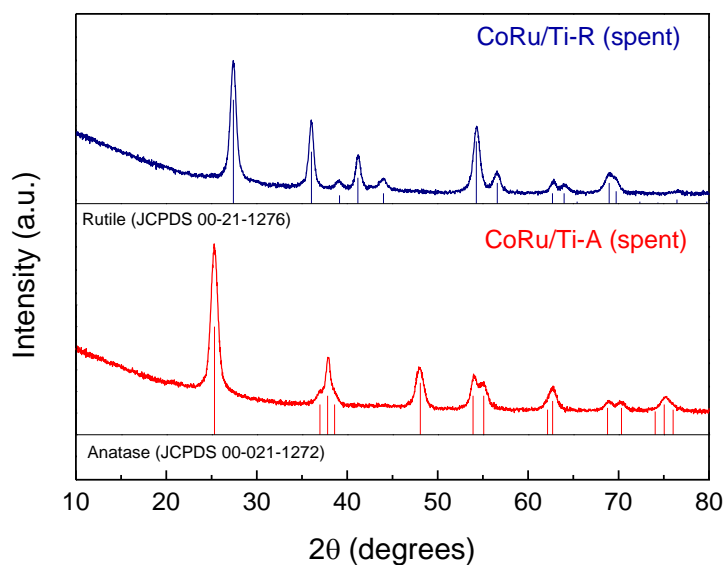
TiO$_2$ PHASES IN SPENT CATALYSTS

Figure S3. XRD patterns for the CoRu/TiO$_2$ catalysts after being used in FTS for ca. 15 h at 220 ºC, 2.0 MPa, and H$_2$/CO= 2. Diffraction lines for pure anatase (JCPDS 00-021-1272) and rutile (JCPDS 00-021-1276) phases are included to facilitate identification of TiO$_2$ phases.

Table S1. Mean size of TiO$_2$ crystallites in the CoRu/TiO$_2$ catalysts before (as-calcined) and after FTS reaction (conditions as in Figure S3) calculated by the Scherrer equation applied to the most intense reflections for anatase (2θ= 25.28°) and rutile (2θ= 27.44°) phases.

Catalyst	Mean TiO$_2$ crystallite size (nm)	
	Before reaction	After reaction
CoRu/Ti-A	11.2	11.5
CoRu/Ti-R	12.0	13.2

These data show negligible variation in the average TiO$_2$ crystallite size (within $\pm$10% error) during the FTS catalytic tests for the studied catalysts.